Beni-Suef University Journal of Basic and Applied Sciences

RESEARCH

Open Access

# Structural control of $V_2O_5$ nanoparticles via a thermal decomposition method for prospective photocatalytic applications

Marwa H. Ashery[1], Mohamed Elnouby[2], E. M. EL-Maghraby[1] and E. M. Elsehly[1*]

## Abstract

**Background** Recently, transition-metal oxides have represented an exciting research topic, especially their fundamental and technological aspects. Here, vanadium pentoxide nanoparticles ($V_2O_5$-NPs) were synthesized through the thermal decomposition of ammonium meta-vanadate. In the current study, we investigated the photocatalytic activity of $V_2O_5$-NPs to develop and regulate the $V_2O_5$ structure for adsorption applications.

**Results** The obtained nanoparticles were inspected by X-ray diffraction, scanning electron microscope, transmission electron microscope, and differential thermogravimetric analysis, which proved the formation of the nanorod structure. The ultraviolet–visible absorption spectra revealed a 2.26 eV band gap for $V_2O_5$-NPs that correlates with indirect optical transitions. The photocatalytic activity of the $V_2O_5$-NPs was investigated by methylene blue (MB) degradation in aqueous solutions. An initial concentration of 25 ppm, a temperature of 40 °C, 40 mg of adsorbent mass, and 1 h of contact time were the optimal conditions for the efficient removal of MB that could reach up to 92.4%. The mechanism of MB photocatalytic degradation by $V_2O_5$-NPs is explained.

**Conclusions** The photodegradation data better fit with the Langmuir isotherm model. The thermodynamic parameters indicated that the adsorption was spontaneous and endothermic. The reaction kinetics followed the pseudo-second-order model. Thermally prepared $V_2O_5$-NPs offer a simple and efficient approach for selective MB removal from an aqueous medium.

**Keywords** $V_2O_5$ nanorods, Thermal decomposition, Photocatalytic degradation, Methylene blue, Dye degradation

*Correspondence:
E. M. Elsehly
elsahli@sci.dmu.edu.eg
Full list of author information is available at the end of the article

**Graphical abstract**

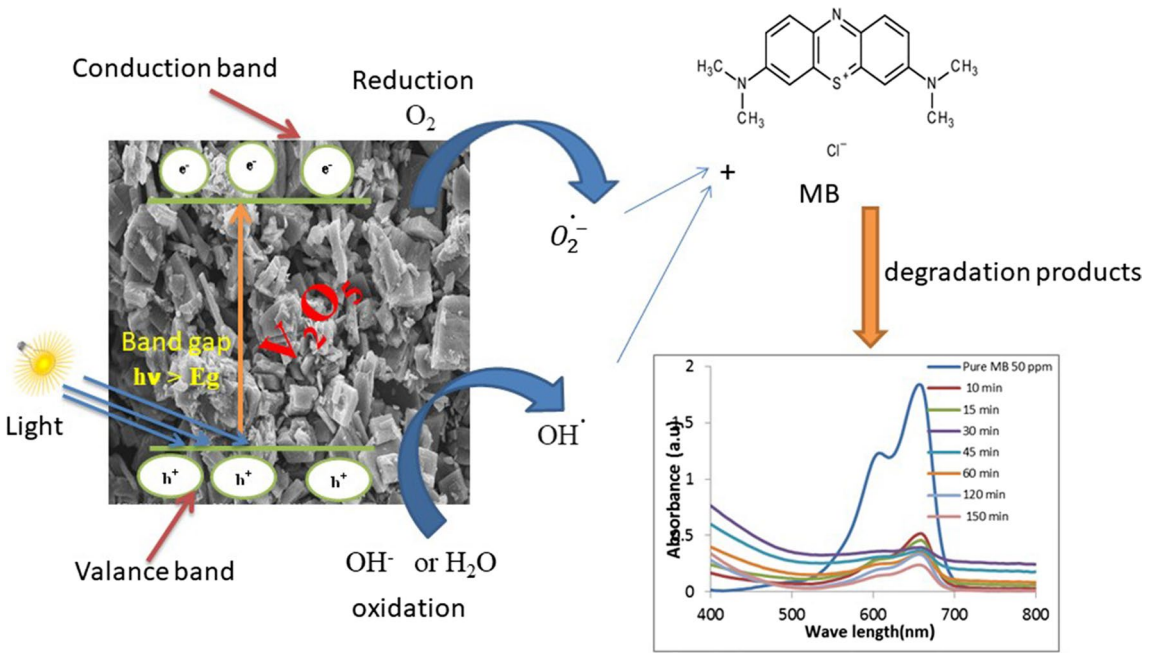


## 1 Background

Owing to their physiochemical features, compared to bulk materials, photocatalysis nanomaterials have attracted significant attention in applied environmental science [1]. Moreover, the term "photocatalysis nanomaterials" dates back nearly 100 years ago and could be simply defined as the change in the rate of a chemical transformation under the action of light in the presence of a catalyst that absorbs light and is involved in the chemical reaction. It has been widely used to mineralize organic compounds as environmental pollutants [2]. Photocatalysis appear to be promising technology with various applications in environmental systems such as air and water purification. The catalyst is activated by interacting with light energy larger than or in the range of the photocatalyst's band gap ($hv \geq E_g$). The band gap or energy gap is an energy range in a solid where no electron states can exist. This is equivalent to the energy required to liberate an outer shell electron from its orbit to move freely within the solid material [3]. These photogenerated electron–hole particles migrate to the semiconductor surface and act to accelerate the reduction and oxidation of adsorbed particles individually [1]. Thermal decomposition (thermolysis) is an important rapid synthetic process to prepare nanomaterials with exceptional properties. Thermal decomposition is an endothermic chemical disintegration that is induced by heat. As a result of this decomposition secondary products are also produced [4]. Recently, transition metal oxides have represented an exciting research topic, especially their fundamental and technological aspects. It contains atoms with unfilled d-shells, which have numerous oxidation states and exhibit mixed-valence phenomena [5]. One of these transition metals is vanadium, which generally subsists in several oxidation states such as (1) $V_nO_{2n+1}$ (e.g. $V_2O_5$), (2) $V_nO_{2n-1}$ (e.g. $V_2O_3$), and (3) $V_nO_{2n}$ (e.g. $V_2O_4$) [6]. Owing to its saturated oxidation state ($V^{+5}$), Vanadium pentoxide ($V_2O_5$) is the main stable compound in these oxidation groups [7]. Owing to its structure, $V_2O_5$ has been incorporated into many applications, including solar cells, optical, and electrical devices [8, 9]. $\alpha$-$V_2O_5$ (Orthorhombic), $\beta$-$V_2O_5$ (tetragonal or monoclinic), and $\gamma$-$V_2O_5$ (Orthorhombic) are some of the polymorphs of $V_2O_5$ [10]. Orthorhombic $\alpha$-$V_2O_5$ is the most stable phase at ambient conditions [11], whereas the $\beta$ and $\gamma$ phases are metastable [7]. $V_2O_5$ has recently gained significant attention due to its unique features, such as catalytic activity, outstanding semiconducting, and electrochemical qualities. Based on the oxidation states variety and the heterogeneity of oxygen coordination geometries, $V_2O_5$ is an excellent catalyst candidate. However, $V_2O_5$ has been the focus of numerous studies because of its scientific curiosity and commercial importance. Among its attractive applications, the photocatalytic activity of

$V_2O_5$ nanoparticles motivates the degradation of hydrocarbons and methylene blue in aqueous solutions [1].

Industrial wastewater effluents, such as paints, leather tanning, and printing, contain a wide range of chemicals that cause pollution to the environment [12–15]. One of the most toxic pollutants is dyes discharged into the environment by the textile and painting industries [16, 17]. Once those dyes metabolize and interact with other contaminants in wastewater, hazardous by-products are produced and affect the aquatic environment and human health [16]. Methylene blue (MB) is commonly used to dye wool and silk, as well as for medicinal purposes to investigate certain illnesses. However, MB-contaminated water is discharged into water resources without treatment. It causes serious ramifications such as vomiting, eye burns, and diarrhea [18]. As a result, developing an effective dye-based treatment approach has become a major research aim [19].

The photocatalytic process is described as the rate change of chemical processes in the presence of a photocatalyst when exposed to light. When a photocatalyst absorbs light quanta, electron–hole pairs are formed, causing chemical modification in reacting materials that make contact with them [20]. The process depends on electron–hole recombination. The hole is large enough to oxidize a wide range of organic pollutants in the water system while also creating the hydroxyl radical $OH^{\bullet}$ [21, 22]. The superoxide radical is formed when electrons in the conduction band interact with oxygen in $H_2O$, which then reacts with the $OH^-$ ion to form $^{\bullet}OH$ radical [23, 24]. Because $^{\bullet}OH$ is a strong oxidizer, it destroys contaminants by oxidizing organic molecules [25, 26].

Herein, the photocatalyst $V_2O_5$-NPs were prepared, and the structure was controlled via the thermal decomposition technique. The obtained nanoparticles were applied as prospective catalyst for Methylene blue degradation. Meanwhile, the thermodynamic studies and photocatalytic mechanism were investigated in detail.

## 2 Materials and methods

### 2.1 Methods

Ammonium metavanadate ($NH_4VO_3$, 99%) was purchased from Sigma Aldrich (Saint Louis, MO, USA), Methylene blue (MB, with the molecular formula $C_{18}H_{18}N_3SC_{l3}H_2O$; $\lambda_{max}$ of 655 nm) was purchased from Chemjet (India) and utilized to prepare the aqueous solution. stock solutions of MB, (50 mg/250 ml), were prepared using distilled water. Double distilled water was employed for the necessary dilutions to create suitable concentrations from the stock solution. The MB concentration before and after each experiment was determined using a UV–Visible spectrophotometer set at 655 nm. The synthesizing of $V_2O_5$ nanoparticles was obtained from the thermal decomposition of ammonium meta-vanadate. DTA-TGA data were collected by the Thermo analyzer (TGA-50 and DTA-50) in the air with a 10 K/min heating rate. The initial mass of the sample was 19.1 mg, and the annealing procedure for $NH_4VO_3$ was conducted at 170 °C, 270 °C, and 450 °C for 1 h. X-ray diffraction (XRD) with monochromatic Cu Ka ($\lambda = 1.5406$ Å) was conducted to investigate the crystallinity. The synthesized nanoparticles morphology was characterized by scanning electron microscopy (SEM, JMS-6010LV) and transmission electron microscopy (TEM, JMS -2100F). Fourier transform infrared spectroscopy (FTIR; Bruker Tensor 37, FTIR spectrophotometer) was used to detect the functional groups. Optical properties and the absorption spectrum were measured by the UV–vis spectrometer (Thermo Scientific Evolution 300) with wavelengths 190–1100 nm. The band gap of each sample was calculated by the following equation [27]:

$$(\alpha h\nu) = A\left(h\nu - \mathrm{Eg}\right)^n \tag{1}$$

where $A$ is a constant where α is the absorbance, $E_g$ is the band gap energy, $(h\nu)$ is the photon energy ($h$ represents the Planck's constant), $A$ is a constant (varies from transition to transition), and n is an index. $n$ takes the values 1/2, 3/2, 2 and 3. The value of $n$ depends on the nature of the electronic transition causing reflection. The Tauc plot is constructed with $h\nu$ on $x$ axis and $(\mathrm{h}\nu\alpha)^{1/2}$on $y$-axis. An extrapolation of this linear region to $(\mathrm{h}\nu\alpha)^2 = 0$ gives the band gap energy of the studied material [3].

### 2.2 Photocatalytic degradation experiments

The photocatalytic degradation of MB by the $V_2O_5$ NPs was used to obtain equilibrium data. The initial dye concentration, contact time, photocatalyst loading, and solution temperature were examined as influences on the photodegradation process. Afterward, 2 ml of degraded MB was collected and analyzed using the spectrophotometer of UV–visible range at 655 nm wavelength.

The dye removal, R%, was estimated using the following equation [28]:

$$R\% = \frac{C_o - C_e}{C_e} * 100 \tag{2}$$

$C_o$ and $C_e$ are the initial and equilibrium liquid phase concentrations, respectively, (mg $l^{-1}$).

The following equation was used to evaluate the quantity of the adsorbed MB, $q_e$ (mg/g) [28].

$$q_e = \frac{(C_o - C_e)V}{m} \tag{3}$$

where $C_0$ and $C_e$ are the initial and equilibrium concentrations of MB, respectively (mg/L), m is the weight of adsorbent in (g) and the solution volume is V (l).

### 2.3 Batch study of photodegradation process

Contact time is one of the most significant factors in the photodegradation process. To investigate the influence of the contact time, 50 mg of the prepared photocatalyst was suspended into a 50 ml aqueous solution of MB (50 ppm, pH = 7) by magnetically stirring at 200 rpm for a period ranging from 15 to 120 min with other constant parameters at room temperature. The effect of concentration on the MB decolorization was investigated at four dye concentrations (100, 50, 25, and 10 ppm) in the presence of 50 mg of the photocatalyst. The removal percentage was controlled by varying adsorbent doses. The main precursor $V_2O_5$, varying as 10, 25, 40, 50, and 100 mg with 50 ml aqueous solution of MB dye 25 mg $l^{-1}$ concentration with other constant parameters. To elucidate the temperature effect on MB dye removal, three different temperatures, 25, 40, and 60°c, were examined with other previously selected parameters. All the experiments were carried out in triplicate and the results were presented as mean ± SD.

### 2.4 Mathematical modeling

#### 2.4.1 The kinetic models

The first and second-order pseudo-kinetic models were used to assess whether the reaction process is chemical or physical [29]. These popular models make the adsorption kinetics and the interaction between adsorbent and adsorbate easier to understand [30]. These kinetic experiments reveal a link between the amount of adsorbate removed and the time required to remove it from an aqueous solution [31]. The pseudo-first-order model was proposed based on the hypothesis that the adsorption rate is proportional to the number of unoccupied adsorption sites. In this model, the adsorption rate was estimated as:

$$\frac{dq}{dt} = K_1(q_e - q_t) \tag{4}$$

where the equilibrium adsorption capacities at a given time are $q_e$ (mg/g) and $q_t$ (mg/g), respectively. $K_1$ ($min^{-1}$) is the first-order kinetic constant.

The second-order pseudo-kinetic model was proposed based on the hypothesis that the adsorption rate is proportional to the square of the number of unoccupied adsorption sites. This model claims that the interactions between the adsorbate and adsorbent are generated by the adsorbate's strong binding to the adsorbent's surface, which can be expressed as [30]:

$$\frac{dq}{dt} = K_2(q_e - q_t)^2 \tag{5}$$

where $K_2$ (g/mg.min) represents the second-order kinetic constant.

#### 2.4.2 Adsorption isotherm models and thermodynamic studies

When the adsorption process achieves equilibrium, an isotherm model explains the mechanism of the adsorption molecules across the solid and liquid phases. The most important isotherm models are Freundlich and Langmuir [23]. Adsorptions occur at predetermined homogeneous regions on the adsorbent, according to the Langmuir model, which is extensively used for monolayer adsorption systems. The Freundlich model supports surface heterogeneity for different energy stages of adsorption sites [28]. The Langmuir isotherm equation is given by [32]:

$$\frac{C_e}{Q_e} = \frac{1}{Q_{max}K_l} + \frac{C_e}{Q_{max}} \tag{6}$$

where $C_e$ is the equilibrium concentration ($mgL^{-1}$), $Q_e$ is the amount of adsorbed dye at equilibrium ($mg.g^{-1}$), $Q_{max}$ ($mg.g^{-1}$) is the Langmuir constants that are related to the adsorption capacity, and $K_L$ (L $mg^{-1}$) is the adsorption rate.

The correlation coefficient, $R^2$, controls the applicability of the isotherm [32]. $R_L$, a dimensionless constant named the separation factor and represented the essential property of the Langmuir isotherm. The viability and nature of adsorption were evaluated by $R_L$ [33], which can be defined by:

$$R_l = \frac{1}{1 + K_l c_o} \tag{7}$$

The $R_L$ value specifies the isotherm type: favorable ($0 < R_L < 1$), linear ($R_L = 1$), irreversible ($R_L = 0$), or unfavorable ($R_L > 1$) [32, 33]. The quantity of the metal adsorption on a given mass of the adsorbent is described by the Freundlich isotherm model. This approach could apply to multi-layer sorption with quasi-adsorption energy and affinity distributions over a wide range of substrates, which takes the form:

$$\ln q_e = \ln K_F + \frac{1}{n} \ln C_e \tag{8}$$

where $k_f$ (l. $mg^{-1}$) and $1/n$ are the Freundlich constants. The slope $1/n$, which ranges from 0 to 1, is an indicator of adsorption ability or surface homogeneity, and it becomes more heterogeneous as it approaches zero [28].

The thermodynamic factors can assess the probability and mechanism of adsorption [34]. The Gibbs free energy ($\Delta G°$), enthalpy ($\Delta H°$), and entropy ($\Delta S°$) are utilized to determine the nature of the adsorption mechanism and the adsorbent suitability [35]. The energy of activation ($E_a$) is critical in establishing whether adsorption is mostly physical or chemical [36]. The thermodynamic parameters were calculated using the given-below equations [37].

$$\Delta G^\circ = -\mathrm{RT}\ln K_\mathrm{d} \tag{9}$$

$$\mathrm{Ln}K_d = \frac{\Delta S^\circ}{R} - \frac{\Delta H^\circ}{Rt} \tag{10}$$

$$K_\mathrm{d} = \frac{q_\mathrm{e}}{C_\mathrm{e}} \tag{11}$$

$R$ is the gas constant (J $\mathrm{mol}^{-1}$ $\mathrm{K}^{-1}$), $\Delta G°$ is the free energy, $K_\mathrm{d}$ is the distribution constant, $T$ is the absolute temperature (K), $q_\mathrm{e}$ is the quantity of dye adsorbed by the adsorbent at equilibrium (mol/L), $C_\mathrm{e}$ is the equilibrium concentration. The $E_a$ defined as the following equation [38]:

$$E_\mathrm{a} = \Delta H^\circ + \mathrm{RT} \tag{12}$$

## 3 Results

### 3.1 Characterization of $V_2O_5$ nanoparticles

The pure $NH_4VO_3$ (TGA–DTA) curves are shown in Fig. 1. The TGA-curve of this sample, as shown in the figure, reveals weight loss processes in the ranges of temperatures 170–230 °C, and 290–500 °C. The initial stage, with 14.82% weight loss, was the thermal disintegration of ammonium meta-vanadate (AMV) into vanadyl chemical species $(NH4)_2V_6O_{16}$. Before the $V_2O_5$ synthesis at 450 °C, the solid product bears the empirical formula of ammonium hexavanadate (AHV) [39]. When the temperature was increased to 450 °C, the sample did not reveal any change in the weight, indicating that the $V_2O_5$ product was stable. Between 400 and 500 °C, the sample exhibits a slight increase in weight. This weight increase could be attributed to the $V^{+4}$ oxidation to $V^{+5}$, which resulted in the creation of yellow crystalline $V_2O_5$.

Figure 2 demonstrates the XRD pattern of $V_2O_5$ prepared at 170 °C, 270 °C, and 450 °C for 1 h. According to the diffraction patterns, the sample at 450°c has sharp peaks at the $2\theta°$ values 15.087°, 19.944°, 20.618°, 25.317°, 30.508°, 31.023°, 33.143°, 47.01, and 50.848° that can be indexed with the planes (200), (001), (101), (201), (400), (301), (111), (600), and (020). These planes were characterized by $V_2O_5$ orthorhombic structure (JCPDS Card No PDF 89–2482), with $a=11.544$ A°, $b=3.571$ A°, and $c=4.383$ A° cell parameters, and unit cell volume = 180.7 A°. The XRD data was refined, along with at reliability factors $R_{wp}=10.32$, $R_{exp}=7.68$, and $\chi^2$ (=1.60). This shows that the observed diffraction peaks properly matched.

To further investigate the functional groups of the synthesized $V_2O_5$ nanoparticles, FTIR spectroscopy in the range of 400–4000 $\mathrm{cm}^{-1}$ was employed. The FTIR spectra of three investigated materials at different temperatures are shown in Fig. 3. As we can see from Fig. 3c, $V_2O_5$-NPs at 450 °C infrared spectrum has multiple bands. Three distinct vibration modes were observed in the FTIR spectra of $V_2O_5$ nanoparticles. The triply coordinated oxygen atom between three vanadium atoms induces a stretching absorption peak of around 475 $\mathrm{cm}^{-1}$ [40]. The bond V–O–V symmetrically stretched around 590 $\mathrm{cm}^{-1}$ [41]. The stretching vibration of the unshared V=O bonds was

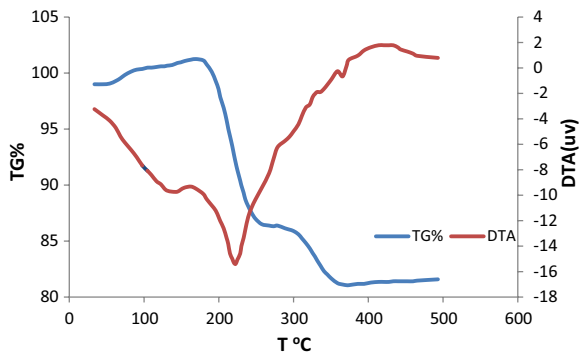


**Fig. 1** Thermogravimetric analysis–differential thermal analysis (TGA–DTA) of pure ammonium vanadate

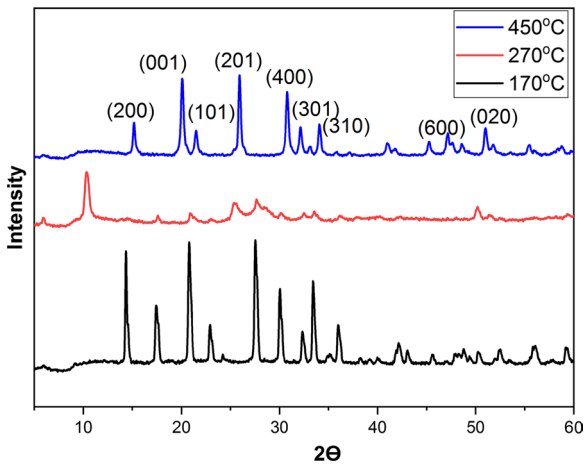


**Fig. 2** The X-ray diffraction of $V_2O_5$ prepared at 170 °C, 270 °C, and 450 °C

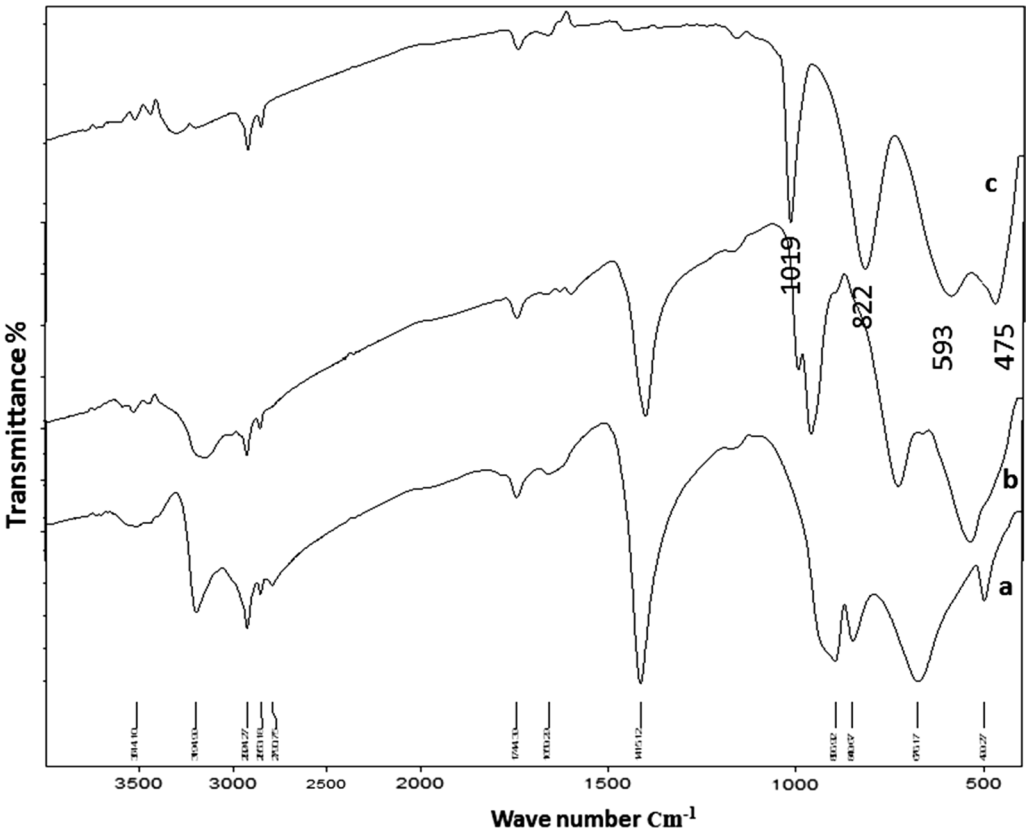


**Fig. 3** FTIR spectra of synthesized $V_2O_5$ at different temperatures 170 °C (a), 270 °C (b) and 450 °C (c)

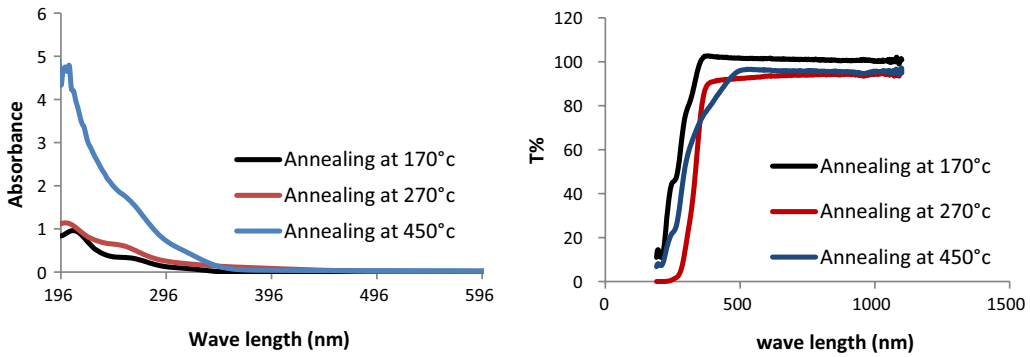


**Fig. 4** Absorption spectra of the sample at different wavelengths on the left side. Ultraviolet–visible (UV–VIS) transmission spectra for samples with different wavelengths on the right side

attributed to the absorption bands at 1020 and 822 $cm^{-1}$, according to previous study [42].

Understanding the electrical nature of the optical band gap of the material may be facilitated by a UV–VIS absorption spectrum spectroscopy [43]. Figure 4 shows a reduction in absorption with increase in the wavelength. The "band gap" refers to a dramatic drop in absorption at low wavelengths [44]. Electronic transitions associated with the sample caused absorption in the near UV area. A significant absorption band at 550 nm corresponded to 2.26 eV in the UV–VIS absorption spectra. The peak within the range of 400–700 nm was displaced to the low-wavelength region, demonstrating a blue shift.

Figure 5 shows the $V_2O_5$ band gaps for the indirectly allowed transitions at 170, 270, and 450 °C which equaled 3.94, 3.16, and 2.26 eV, respectively. The disturbance of

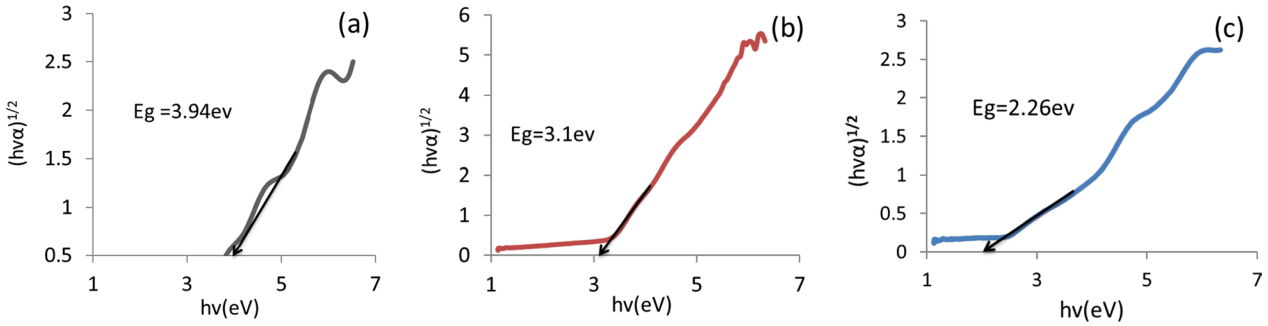


**Fig. 5** Energy gaps for $V_2O_5$ at temperature values of 170 °C (**a**), 270 °C (**b**), and 450 °C (**c**)

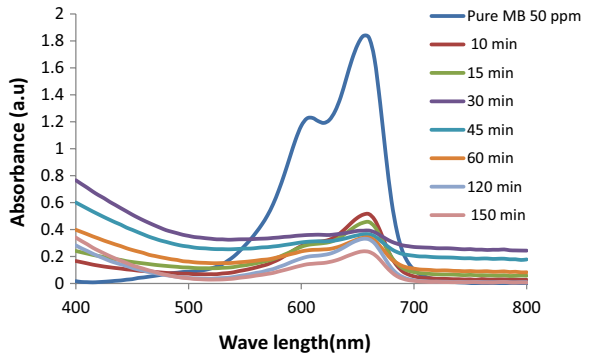


**Fig. 6** Variation in the absorption spectra of MB on $V_2O_5$ at various times

electrons caused by incoming light and the transition between electronic states are the sources of the optical property of a material [45]. In $V_2O_5$, 3*d* bands of vanadium constitute the conduction band, while 2*p* bands of oxygen form the valence band.

## 3.2 Photodegradation of methylene blue

### *3.2.1 Effect of contact time*

Over 150-min time intervals; the effect of contact time on the photodegradation process of MB by the $V_2O_5$-NPs was examined. Figure 6 shows the change in the optical absorption of the aqueous MB solution by $V_2O_5$-NPs under a light spectrum. The intensity of the absorption peak at 655 nm gradually decreased with an increase in time, indicating that MB had been photodegraded by the $V_2O_5$ catalyst. As shown in Fig. 7a, with an increase in contact time, the quantity of MB adsorbed increased until it reached its maximum value after 45 min. It may take up to 60 min for the dye to be completely absorbed by the prepared material. Therefore, within 45 min, the maximal dye elimination by the $V_2O_5$ powder was achieved, and the system attained equilibrium.

### *3.2.2 Influence of the initial dye concentration on the MB dye removal*

Figure 7b depicts the effect of dye concentration on the Photodegradation efficiency of MB. The effective removal of the MB dye increased with an increase in dye concentration during photodegradtion by the $V_2O_5$-NPs. The highest removal percentage was recorded at the initial concentration of 25 ppm to reach 92.4%. Then the removal percentage decreased at the concentrations of 50 and 100 ppm to 77.8% and 45.6%, respectively.

### *3.2.3 Photoadsorbent dosage and removal efficiency*

Figure 7c shows the adsorbent mass impact on the MB removal from an aqueous solution by photocatalytic degradation. As shown in Fig. 7c, the MB removal efficiency increased from 48.5 to 92.4% with the addition of $V_2O_5$-NPS when the photodsorbent dose was increased from 10 to 100 mg, indicating that additional adsorption sites were accessible. For future investigations, a 40 mg adsorbent dosage was adopted. The transfer of dye ions to active adsorption sites was be constrained at large adsorbent doses, thereby lowering the removal efficiency [46].

### *3.2.4 Temperature dependence of MB removal*

The solution temperature considerably impacts the photodegradation procedure, where any variation in the temperature might disrupt the equilibrium research [47]. The influence of solution temperature on MB Photodegradation efficiency is illustrated in Fig. 7d. It was revealed that when the temperature increased, the removal efficiency also increased. It can be stated that when dye mobility increased, the interaction with the active areas on the surface of the adsorbent improves [48]. A temperature of 40 °C was selected for subsequent equilibrium studies because of the efficient removal attained at this temperature.

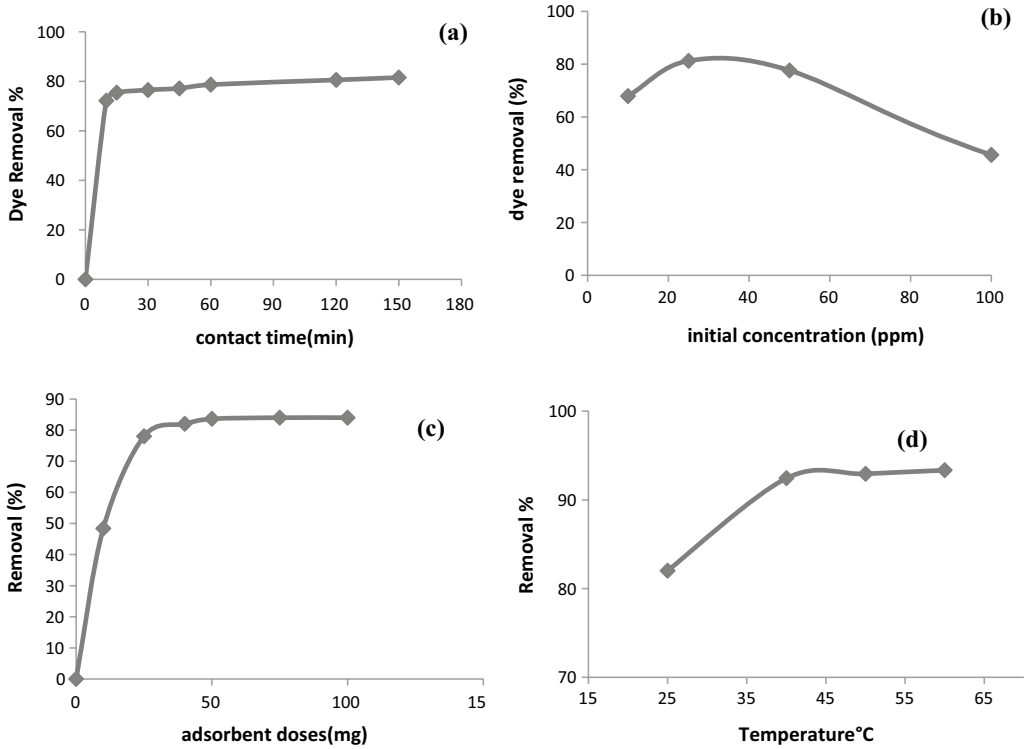


**Fig. 7** Degradation percentage versus contact time of $V_2O_5$ (**a**). Variation in the initial concentration of methylene blue (MB) during its photodegradation by $V_2O_5$ (contact time = 60 min, pH = 7, and $T$ = 25 °C ± 2 °C) (**b**). Influence of the dose on the adsorption of MB (initial concentration = 25 ppm, temperature = 25 °C ± 2 °C, shaking speed = 200 rpm, and pH = 7) (**c**). Temperature effect on the removal at an initial concentration of MB of 25 ppm (contact time = 60 min and pH = 7) (**d**)

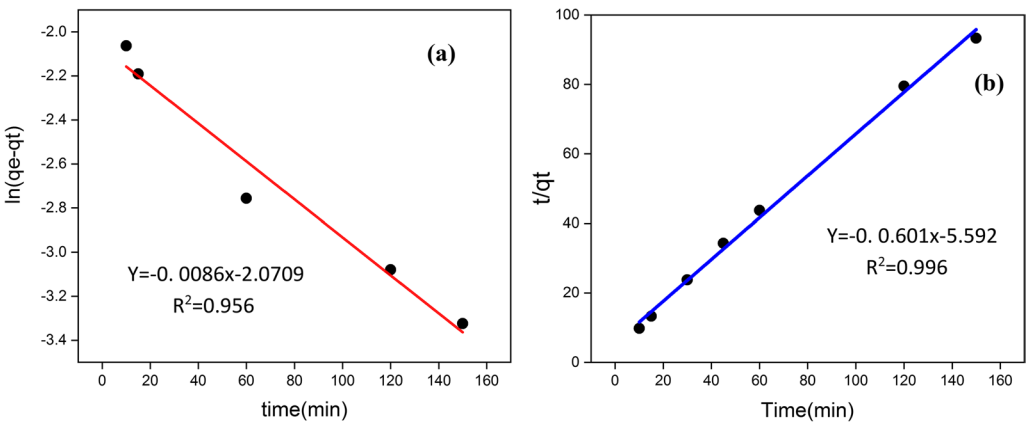


**Fig. 8** Pseudo-first-order kinetic reaction (**a**) Pseudo-second -order reaction (**b**)

### 3.3 Kinetic studies of MB degradation

To determine the sorption mechanism, various models can demployed [49]. Here, we employed the pseudo-first- and pseudo-second-order models because they are more widely applicable than other adsorption models. Figure 8a shows the pseudo-first-order kinetic response as a linear relationship between $\log(q_t - q_e)$ with time ($t$). The pseudo-second-order reaction is shown in Fig. 8b, which reveals a positive relationship between $t/q_t$ and time. Table 1 shows the kinetic constants ($q_e$, $K_1$, and $K_2$) derived from the slope and intercept of the regression equations.

The correlation factor was 0.996 for the pseudo-second-order model, Table 1: it was higher than those of

**Table 1** Pseudo-first and second-order kinetic constants with correlation coefficients

| Removal process | | Pseudo-first-order | | | Pseudo-second-order | | |
|---|---|---|---|---|---|---|---|
| | $q_e$, (exp)mg/g | $K_1$, $min^{-1}$ | $q_e$, mg $g^{-1}$ | $R^2$ | $K_2$, g $mg^{-1}$ $min^{-1}$ | $q_e$, (mg $g^{-1}$) | $R^2$ |
| Photodegradation | 1.44 | 0.009 | 0.126 | 0.956 | 0.0645 | 1.663 | 0.996 |

**Table 2** Isotherm parameters of the Langmuir and Freundlich of MB by $V_2O_5$ photocatalytic

| Isotherm model | Isotherm parameters | | | $R^2$ |
|---|---|---|---|---|
| Langmuir | $Q_{max}$ (mg $g^{-1}$) = 1.267 | $K_l$ (L $mg^{-1}$) = 5.320 | $R_l$ = 0.0019–0.018 | 0.9988 |
| Freundlich | $K_f$ (mg $g^{-1}$)(L $mg^{-1})^{1/n}$ = 1.321 | | 1/*n* = 0.278 | 0.8570 |

the first-order model. The information obtained showed that the pseudo-first-order model failed to illustrate the adsorption capacity, $q_e$, where the pseudo-second-order model could describe MB adsorption upon photocatalysis. In addition, the adsorption capabilities estimated using the pseudo second-order model were similar to those obtained through experiments. The adsorption capabilities derived using the pseudo-first-order model, otherwise, did not match the experimental results. Consequently, the MB adsorption can be represented as a pseudo-second-order model, indicating that the MB adsorption can be described as chemical adsorption.

### 3.4 Adsorption isotherm

MB adsorption was investigated using $V_2O_5$-photocatalysis at various initial concentrations. Table 2 shows the parameters and the relevant correlation coefficients of the two isotherms. The Langmuir model yielded the equilibrium adsorption data better than the Freundlich model, based on the obtained high correlation coefficients ($R^2$). $C_e/q_e$ is plotted versus $C_e$ in Fig. 9a, providing a straight line with $R^2 = 0.996$, suggesting that the Langmuir model suited the adsorption data well. The slope of the linear plot yielded the value of $q_{max}$ of 1.267 mg/g, while the intercept yielded the value of $K_L$ (Table 1). The MB separation factor ($R_L$)

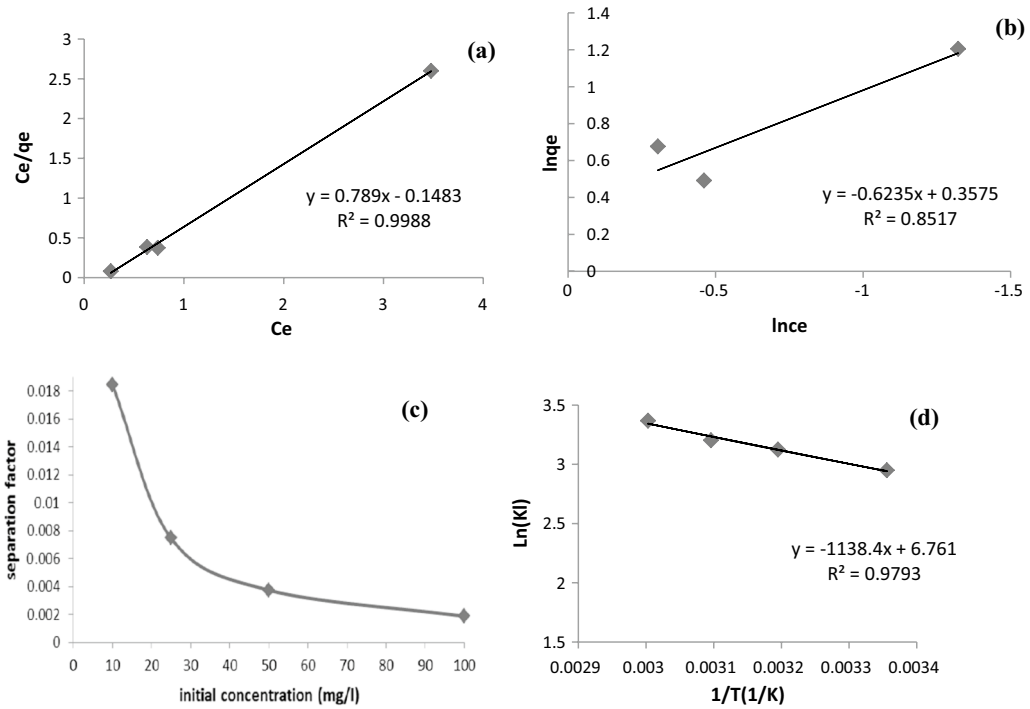


**Fig. 9** Plots of MB adsorption using the Langmuir isotherm at various starting concentrations (**a**), the Freundlich isotherm at various beginning concentrations (**b**), separation factor for MB adsorption (**c**). lnK versus 1/T obtained for the Photodegradation of Methylene blue by $V_2O_5$ (**d**)

was calculated using Eq. (6) at various starting metal concentrations (Fig. 9c). Table 2 shows that the values of $R_L$ for MB adsorption by $V_2O_5$ photocatalytic were in the range of 0.0019–0.018. The adsorption of MB onto the $V_2O_5$ adsorbent was found to be favorable, with an $R_L$ value ranging from 0 to 1. As shown in this table, the Langmuir isotherm data reveals the rapid filling of the material's active sites. The resulting data also illustrated that the chemisorption and monolayer adsorption processes of sorbate on the adsorbent surface were highlighted using the Langmuir isotherm. The Freundlich isotherm model has a good correlation coefficient, which might imply its adaptability.

### 3.5 Thermodynamic studies

The slope and intercept of the $\ln(K_d)$ against $1/T$ plot, Fig. 9d, were used to calculate $\Delta S^\circ$ and $\Delta H^\circ$ values. The negative value obtained for $\Delta G^\circ$ indicated that the adsorption was spontaneous and favorable. With increase in temperature, the negative value of $\Delta G$ decreased, indicating that the Photodegradation of Methylene blue on $V_2O_5$-NPs was favorable [51]. The obtained $\Delta G$ values were lower than 20 kJ/mol, suggesting that the adsorption rate follows a physical adsorption mechanism. The enthalpy ($\Delta H^\circ$) indicated whether the process is exothermic or endothermic, and distinguishes between chemical and physical adsorption systems [30]. As a result, the positive value of $\Delta H^\circ$ (9.465 kJ/mol), Table 3, indicated that the removal of MB was an endothermic process, whereas the low value of this energy (< 40 kJ/mole) indicates that it was physisorption [52]. The increased diffusion rate of adsorbate across the exterior boundary and the interior pores of adsorbents might explain this phenomenon [53]. During the adsorption phase, the value of $\Delta S$ was positive, suggesting randomness existed in the system solid/solution interface [54]. The resulting $E_a$ value is less than 40 kJ/mol, which confirms the inferred physisorption process [52].

## 4 Discussion

According to the DTA curve of AMV, (Fig. 1), the sample heated in air exhibited two endothermic peaks. The endothermic peak at 130 °C, could specify the loss of water. At 218 °C, a second peak corresponded to the loss of water and ammonia during the degradation process that led to the production of AHV. Without detecting any weight changes in the TGA-curve, the high and abrupt exothermic peak, its maxima, positioned at 360 °C, was observed. Such a peak could be related to $V_2O_5$ crystallization [55]. The formations of the intermediates were atmosphere-dependent stages [56]. The main weight loss occurred because of the desertion of $NH_3$ and $H_2O$ during the thermal decomposition of $NH_4VO_3$ as follows [57]:

$$2NH_4VO_3 \rightarrow V_2O_5 + 2NH_3 + H_2O \quad (13)$$

Sequences of chemical processes are required to produce $V_2O_5$ from AMV. The immediate removal of water and ammonia represents the initial step in this process. Exothermic and endothermic processes were involved in the second stage of decomposition. The exothermic process was compatible with the degradation of ammonia on the surface of vanadium pentoxide, and the endothermic reaction might be the release of water [58].

The material's band gap energy ($E_g$) is one of the essential distinctive parameters regarding its properties. The $E_g$ of semiconductors or insulators reveals a marked decrease with the temperature rising. The fluctuation in the $E_g$ value is critical for basic research and practical applications [59, 60]. The fundamental absorption in crystalline $V_2O_5$ is mostly due to the change from oxygen *p*-type to a vanadium 3*d*-type wave-function [61]. The current study confirms that the band gap value of $V_2O_5$ is 2.26 eV due to indirect optical transitions, as previously reported which recorded the band gap of $V_2O_5$ in the range of 2.15–2.65 eV [62].

SEM images were taken at different temperatures (170, 270, and 450 °C) to investigate the surface and the morphology of thermally treated AMV (Fig. 10). It is revealed that ammonium Meta vanadate heated at 170 °C attained an average particle size of 2.06 µm (Fig. 10a). In addition, when the temperature reaches 270 °C, the shape of the particles change from the rectangular plate with sharp edge (Fig. 10a) [63]. It is assumed that the agglomerated shape and rectangular plate may be attributed to the formation of ammonium Hexa vanadate with an average particle size of 1.462 µm. The surface morphologies of the products and structural information at different

**Table 3** The thermodynamic parameters for the MB removal

| Adsorbent | Adsorbate | Temp(K) | Kd | $\Delta G^\circ$ (kJ mol$^{-1}$) | $E_a$ (KJmol$^{-1}$) | $\Delta S^\circ$ (kJ mol$^{-1}$ K) | $\Delta H^\circ$ (kJ mol$^{-1}$) |
|---|---|---|---|---|---|---|---|
| $V_2O_5$ | MB | 298 | 19.103 | − 7.309 | 11.924 | 56.211 | 9.465 |
| | | 313 | 22.739 | − 8.129 | 12.067 | | |
| | | 323 | 24.594 | − 8.600 | 12.150 | | |
| | | 333 | 29.006 | − 9.323 | 12.233 | | |

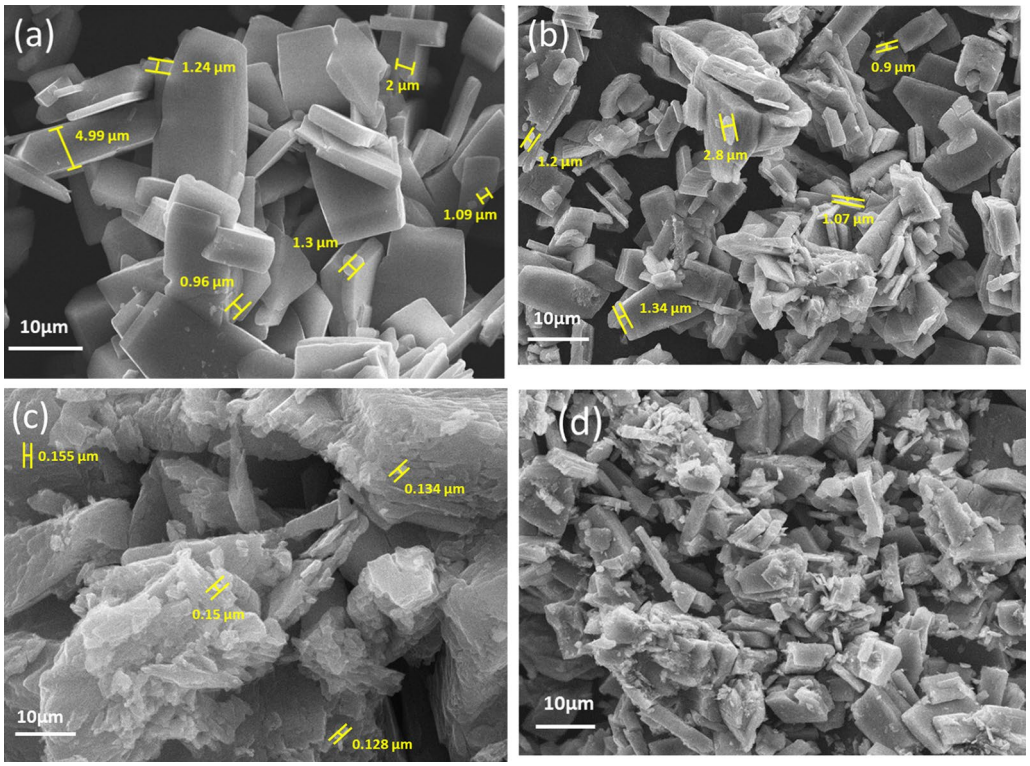


**Fig. 10** SEM images of thermally treated AMV at $T = 170$ °C (**a**), $T = 270$ °C (**b**), and 450 °C (**c**, **d**)

magnifications are illustrated in Fig. 10c, d. The nanostructured $V_2O_5$ particles fabricated under thermal decomposition at 450 °C for 1 h, include nanorods of nonuniform $V_2O_5$ crystals and rectangular plates. Furthermore, most agglomeration attained an average particle size of 0.153 µm. Vanadium oxide nanoparticles appear in the form of a black powder.

TEM and HRTEM images show the morphologies of thermal decomposition of $NH_4VO_3$ at 170 °C, 270 °C, and the prepared $V_2O_5$ powders treated at $T = 450$ °C, respectively (Fig. 11). As can be seen from the figure the lattice fringes of $V_2O_5$ in the range of $d = 0.19$ nm.

Figure 12 shows the FTIR spectra of MB solution prior to and after $V_2O_5$ decomposition. The MB dye exhibited a distinctive peak associated with the functional groups in the MB dye consisting of CH=N at 1615 $cm^{-1}$ prior to degradation (Fig. 12a). The FTIR spectrum exhibited a new peak after photocatalytic degradation of the MB dye. The V=O symmetric stretching was responsible for the bands at 1030 $cm^{-1}$, whereas V–O–V stretching is responsible for the bands at 850 $cm^{-1}$, Fig. 12b [63]. Furthermore, due to the absorption of MB on $V_2O_5$, the FTIR peak of CH=N changed from 1615 to 1655 $cm^{-1}$.

As indicated in Fig. 6, the proportion of MB removed raised significantly as contact time increased. The findings imply that the initial rate of adsorbate removal enhanced with the increased surface area of the adsorbent available for dye ion adsorption. Due to lower active sites on the sorbent surface, only a minor increase in dye removal was detected after a specific duration [64]. When a dye concentration of 50 ppm was used, the agitation time of 60 min appeared to be sufficient to attain equilibrium.

When the dye concentration increased, the photodecolorization, i.e., MB dye removal, increased. The generation of hydroxyl radicals ($OH^{\bullet}$), which might react with dye molecules, is linked to these findings. As the MB concentration increased, the catalyst's active sites became coated with dye ions, which causes a decrease in the removal efficiency. Thus, the production of hydroxyl radicals ($OH^{\bullet}$) on the surface of catalyst was reduced, and the path length of photons entering the dye solution was reduced [65].

The performance of synthesized $V_2O_5$ is compared with other materials for the degradation of MB. Table 4 shows a comparison of the photocatalytic performance of some photocatalysts for the degradation of Methylene blue. Compared with published results, our study offers a simple and efficient approach to selectively remove MB from an aqueous medium, with a detailed thermodynamic study.

Three phases are generally involved in the photocatalytic process. The dye molecules travel from the aqueous

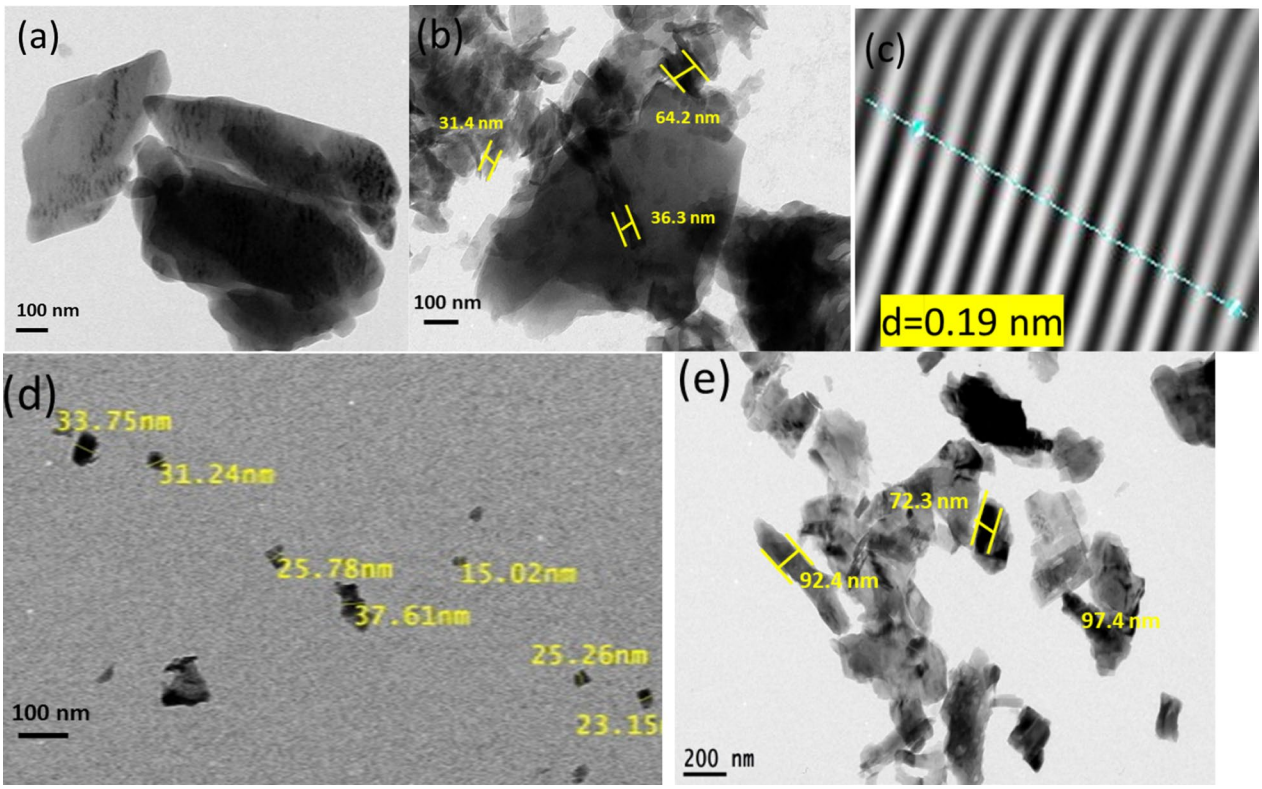


**Fig. 11** TEM and HRTEM images of thermally treated ammonium Meta vanadate at $T = 170$ °C (**a**), $T = 270$ °C (**b**) and at $T = 450$ °C (**c**–**e**)

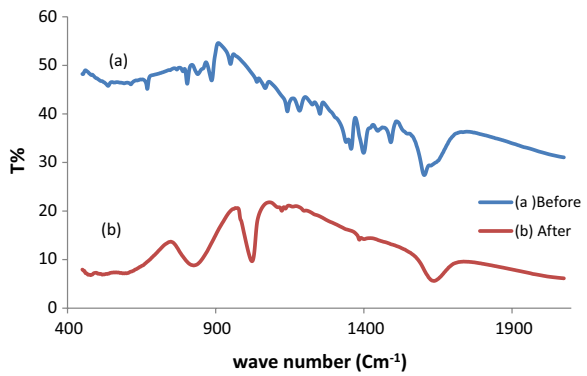


**Fig. 12** The FTIR spectra for MB prior to (**a**) and after degradation (**b**)

solution to the external surface of the catalyst during the first diffusion layer of the dye. Intraparticle diffusion is the second inner diffusion, in which dye molecules are absorbed from the external layer to inside the catalyst pores. Finally, the dye molecules connect with the active sites of the interior pores of the catalyst during the third stage [1]. Figure 13 shows a schematic of the photodegradation phenomena. When a photon with an energy of at least 2.3 eV interacted with the photocatalyst $V_2O_5$-NPs, an electron–hole pair is formed. In this situation, electrons ($e^-$) were stimulated from the valence band to the conduction band whereas holes ($h^+$) are created in the valence band [54]:

**Table 4** comparison of the photocatalytic performances of certain photocatalysts for the degradation of methylene blue (MB)

| Catalyst | Photodegradation efficiency (%) | Dye initial concentration | The catalyst dose (mg) | Light source | Degradation time | Temperature (°C) | References |
|---|---|---|---|---|---|---|---|
| $V_2O_5$-NPs | 81 | 10 mg/l | 50 | Visible light | 2 h | 25 | [47] |
| CdS nanorods | 92.5 | $1 \times 10^{-5}$ M | 100 | Visible light | 25 min | 25 | [48] |
| NGP/$V_2O_5$ | 75 | 20 mg/l | 400 | Visible light | 120 min | 25 | [61] |
| ZnO-NPs | 96 | 40 mg/l | 200 | Visible light | 60 min | 25 | [49] |
| $MnTiO_3/TiO_2$ | 75 | $1 \times 10^{-5}$ M | 50 | Sunlight irradiation | 240 min | 25 | [50] |
| $V_2O_5$/ZnO | 97 | 500 mg/l | 500 | Visible light | 120 min | 25 | [51] |
| $V_2O_5$-nanorods | 92.4 | 25 mg/l | 40 | Light spectrum | 60 min | 40 | This work |

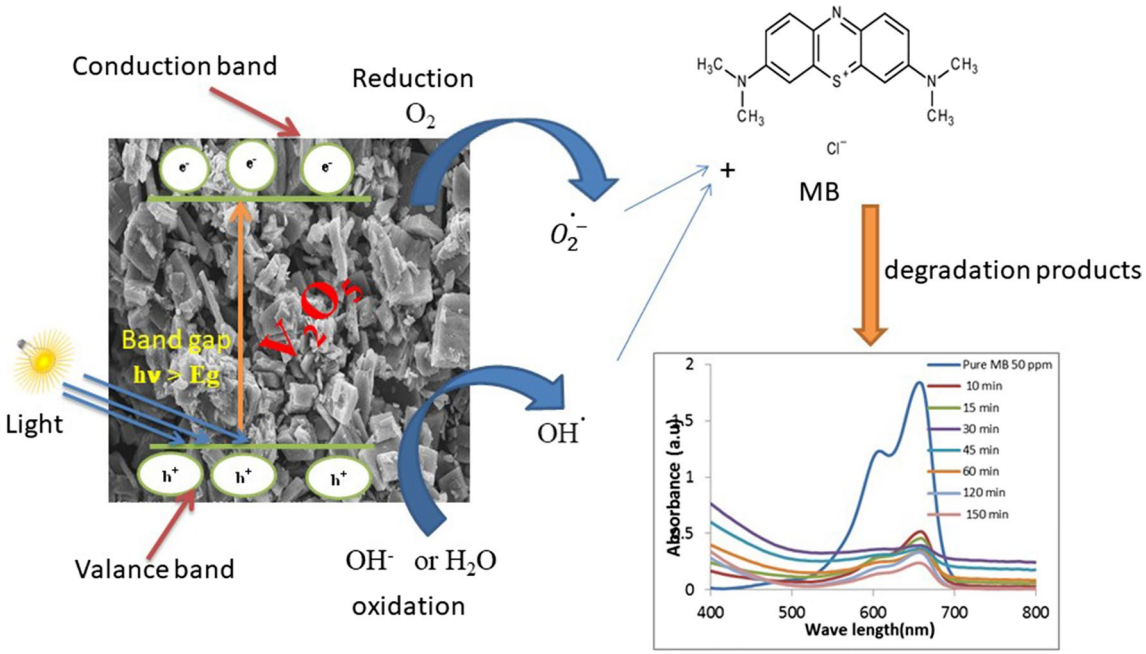


**Fig. 13** The proposed mechanism involved in the photocatalytic activities of $V_2O_5$-NPs

$$V_2O_5 - NPs + hv \rightarrow e^-_{CB} + h^+_{VB} \quad (14)$$

where hv denotes the energy required to transport an electron from the VB to the CB.

Irradiated electrons might be easily captured by $O_2$ absorbed on the photocatalyst surface, resulting in superoxide radicals $\left(O_2^{\bullet-}\right)$, $e^-_{CB} + O_2 \rightarrow O^{\bullet-}$. Thus, $O^{\bullet-}$ might interact with $H_2O$ to form the hydroperoxy radical $\left(HO_2^{\bullet}\right)$ and hydroxyl radical ($OH^{\cdot}$), which are powerful oxidizing mediators that can degrade organic molecules. Simultaneously, surface hydroxyl groups on the photocatalyst surface might trap the photoinduced holes, resulting in hydroxyl radicals $OH^{\bullet}$. Finally, oxidizing the organic molecules will produce carbon dioxide and water. Moreover, positive hole and electron recombination may occur, lowering the photocatalytic activity of the produced nanocatalyst.

## 5 Conclusion

$V_2O_5$ nano-rods were successfully synthesized by thermal decomposition. The TEM and SEM of $V_2O_5$-NPs revealed its rod-like shape. $V_2O_5$ particles were generated by decomposition at 450 °C for 1 h had a particle size of 0.153 µm and a lattice fringe of $d = 0.19$ nm. According to the UV–VIS absorption spectrum, $V_2O_5$ had a band gap of 2.26 eV. The Photocatalytic activity of the synthesized $V_2O_5$ nano-rods was examined by selectively removing of MB from an aqueous medium under light spectrum. The quantity of adsorbed MB is correlated with the solution temperature, initial dye concentration, adsorbent dose, and contact duration. Under visible light, the $V_2O_5$ nano-rods exhibited an efficient degradation of MB dye within 60 min. The obtained adsorption data fit the Langmuir isotherm model. The reaction kinetics followed the pseudo-second-order model. This study offers a simple and effective photocatalyst approach for the effective removal of various dyes from polluted solutions.

**Abbreviations**

| | |
|---|---|
| XRD | X-ray diffraction |
| SEM | Scanning electron microscope |
| TEM | Transmission electron microscope |
| DTA | Differential thermogravimetric analysis |
| FTIR | Fourier–transform infrared spectroscopy |
| MB | Methylene blue |
| $V_2O_5$ | Vanadium pentoxide |
| α-$V_2O_5$ | Orthorhombic vanadium pentoxide |
| AMV | Ammonium metavanadate |
| AHV | Ammonium hexavanadate |
| NPs | Nanoparticles |

**Acknowledgements**
Thanks to the Faculty of Science, Physics department, Damanhour University, Egypt.

**Author contributions**
MA, E. Elsehly, EME, and ME contributed to the conception and design of the study. Data collection, analysis, and manuscript preparation were performed by E. Elsehly. E. Elsehly, MA and ME wrote the first draft of the manuscript. EME and E. Elsehly revised the manuscript, participate on the discussion and analysis of the data. All the authors commented on previous editions of the manuscript. All authors read and approved the final manuscript.

**Funding**
This study was funded by the Academy of Scientific Research and Technology (ASRT), Egypt, Grant No. 6735.

**Availability of data and materials**
All data and other supplementary materials are already included in the main manuscript.

## Declarations

**Ethics approval and consent to participate**
Not applicable.

**Consent for publication**
Not applicable.

**Competing interests**
The authors declare that they have no competing interest in this study.

**Author details**
[1]Physics Department, Faculty of Science, Damanhour University, Damanhour 22516, Egypt. [2]Nanomaterials and Composites Research Department, Advanced Technology and New Materials Research Institute (ATNMRI), City for Scientific Research and Technological Applications (SRTA-City), New Borg El-Arab City, Alexandria 21934, Egypt.

Received: 1 July 2022 Accepted: 17 January 2023
Published online: 28 January 2023

**References**

1. Sajid M, Akhtar Shad N, Javed Y, Khan S, Zhang Z et al (2020) Preparation and characterization of Vanadium pentoxide ($V_2O_5$) for photocatalytic degradation of monoazo and diazo dyes. Surf Interfaces 19:100502
2. Jacob R, Nair HG, Isac J (2014) Optical band gap analysis of nano-crystalline ceramic PbSrCaCuO. J Adv Phys 5:816–822
3. Vinila V, Isac J. Analysis of bandgap energy and refractive index of ferroelectric perovskite Pbbatio3, 2018
4. Baykara SZ (2004) Hydrogen production by direct solar thermal decomposition of water, possibilities for improvement of process efficiency. Int J Hydrogen Energy 29:1451–1458
5. Kazakova E, Berezina O, Kirienko D, Markova N (2014) Vanadium oxide gel films: optical and electrical properties, internal electrochromism and effect of doping. J Sel Top Nano Electron Comput 2:7–19
6. Huotari J, Lappalainen J, Eriksson J, Bjorklund R, Heinonen E et al (2016) Synthesis of nanostructured solid-state phases of $V_7O_{16}$ and $V_2O_5$ compounds for ppb-level detection of ammonia. J Alloys Compd 675:433–440
7. Asadov A, Mukhtar S, Gao W (2015) Crystal structure development of vanadium oxide thin films deposited by a magnetron sputtering technique. J Vacuum Sci Technol B Nanotechnol Microelectron Mater Process Meas Phenom 33(4):041802
8. Nair DP, Sakthivel T, Nivea R, Eshow JS, Gunasekaran V (2015) Effect of surfactants on electrochemical properties of vanadium-pentoxide nanoparticles synthesized via hydrothermal method J Nanosci Nanotechnol 15:4392–4397
9. Bera B, Das P, Bhattacharya M, Ghosh D, Mukhopadhyay A, Dey A (2015) Nanoscale contact resistance of $V_2O_5$ xerogel films developed by nanostructured powder. J Phys D Appl Phys 49(8):085303
10. Prześniak-Welenc M, Łapiński M, Lewandowski T, Kościelska B, Wicikowski L, Sadowski W (2015) The influence of thermal conditions on $V_2O_5$ nanostructures prepared by sol–gel method. J Nanomater 2015:3
11. Balog P, Orosel D, Cancarevic Z, Schön C, Jansen M (2007) $V_2O_5$ phase diagram revisited at high pressures and high temperatures. J Alloys Compd 429:87–98
12. Barjasteh-Moghaddam M, Habibi-Yangjeh A (2011) Effect of operational parameters on photodegradation of methylene blue on ZnS nanoparticles prepared in presence of an ionic liquid as a highly efficient photocatalyst. J Iran Chem Soc 8:S169–S175
13. Gajbhiye SB (2012) Photocatalytic degradation study of methylene blue solutions and its application to dye industry effluent. Int J Mod Eng Res 2:1204–1208
14. Elsehly EM, Chechenin NG, Makunin AV, Shemukhin AA, Motaweh HA (2020) Surface functionalization of multi-walled carbon nanotubes by ozone and the enhancement of their environmental applications. Nano Express 1(2):020023. https://doi.org/10.1088/2632-959X/abaafd
15. Elsehly EM, Chechenin NG, Makunin AV, H.A. (2016) Motaweh, morphological and structural modifications of multiwalled carbon nanotubes by electron beam irradiation. Mater Res Express 3:105013
16. Akpan UG, Hameed BH (2009) Parameters affecting the photocatalytic degradation of dyes using $TiO_2$-based photocatalysts: a review. J Hazard Mater 170:520–529
17. Houas A, Lachheb H, Ksibi M, Elaloui E, Guillard C, Herrmann J-M (2001) Photocatalytic degradation pathway of methylene blue in water. Appl Catal B 31:145–157
18. Salehi M, Hashemipour H, Mirzaee M (2012) Experimental study of influencing factors and kinetics in catalytic removal of methylene blue with $TiO_2$ nanopowder. Am J Environ Eng 2:1–7
19. Elsehly EM (2020) Enhanced removal of Ni(II) from aqueous solutions by effective acid functionalization of carbon nanotube based filters. Egypt J Chem 63:3861–3871
20. Kadhim RF (2017) Photocatalytic removal of methylene blue dye by using of ZnS and CdS. Iraqi J Phys (IJP) 15:11–16
21. Sajid MM, Shad NA, Javed Y, Khan SB, Imran Z et al (2019) Fast surface charge transfer with reduced band gap energy of $FeVO_4$/graphene nanocomposite and study of its electrochemical property and enhanced photocatalytic activity. Arab J Sci Eng 44:6659–6667
22. Zhou F, Zhao X, Yuan C, Li L (2008) Vanadium pentoxide nanowires: hydrothermal synthesis, formation mechanism, and phase control parameters. Cryst Growth Des 8:723–727
23. Chen F, Huang H, Guo L, Zhang Y, Ma T (2019) The role of polarization in photocatalysis. Angew Chem Int Ed 58:10061–10073
24. Chetty EC, Dasireddy VB, Maddila S, Jonnalagadda S (2012) Efficient conversion of 1, 2-dichlorobenzene to mucochloric acid with ozonation catalyzed by $V_2O_5$ loaded metal oxides. Appl Catal B 117:18–28
25. Sajid MM, Khan SB, Shad NA, Amin N (2018) Synthesis of $Zn_3(VO_4)_2$/$BiVO_4$ heterojunction composite for the photocatalytic degradation of methylene blue organic dye and electrochemical detection of $H_2O_2$. RSC Adv 8:35403–35412
26. Sajid MM, Khan SB, Shad NA, Amin N, Zhang Z (2018) Visible light assisted photocatalytic degradation of crystal violet dye and electrochemical detection of ascorbic acid using a $BiVO_4$/$FeVO_4$ heterojunction composite. RSC Adv 8:23489–23498
27. Avansi W, de Mendonça VR, Lopes OF, Ribeiro C (2015) Vanadium pentoxide 1-D nanostructures applied to dye removal from aqueous systems by coupling adsorption and visible-light photodegradation. RSC Adv 5:12000–12006
28. Geçgel Ü, Özcan G, Gürpınar GÇ (2013) Removal of methylene blue from aqueous solution by activated carbon prepared from pea shells (Pisum sativum). J Chem 2013:614083. https://doi.org/10.1155/2013/614083
29. Sadeghalvad B, Azadmehr A, Hezarkhani A (2016) Enhancing adsorptive removal of sulfate by metal layered double hydroxide functionalized Quartz-Albitophire iron ore waste: preparation, characterization and properties. RSC Adv 6:67630–67642
30. Song G, Zhu X, Chen R, Liao Q, Ding Y-D, Chen L (2016) An investigation of $CO_2$ adsorption kinetics on porous magnesium oxide. Chem Eng J 283:175–183
31. Jabar JM, Odusote YA, Alabi KA, Ahmed IB (2020) Kinetics and mechanisms of congo-red dye removal from aqueous solution using activated *Moringa oleifera* seed coat as adsorbent. Appl Water Sci 10:1–11
32. Kuang Y, Zhang X, Zhou S (2020) Adsorption of methylene blue in water onto activated carbon by surfactant modification. Water 12:587
33. Rao HJ, King P, Kumar YP (2018) Equilibrium isotherm, kinetic modeling, and characterization studies of cadmium adsorption in an aqueous solution by activated carbon prepared from bauhinia purpurea leaves. Rasayan J Chem 11:1376–1392
34. Rakass S, Oudghiri Hassani H, Mohmoud A, Kooli F, Abboudi M et al (2021) Highly efficient methylene blue dye removal by nickel molybdate nanosorbent. Molecules 26:1378

35. Edet UA, Ifelebuegu AO (2020) Kinetics, isotherms, and thermodynamic modeling of the adsorption of phosphates from model wastewater using recycled brick waste. Processes 8:665
36. Ma J, Jia Y, Jing Y, Yao Y, Sun J (2012) Kinetics and thermodynamics of methylene blue adsorption by cobalt-hectorite composite. Dyes Pigm 93:1441–1446
37. El Essawy NA, Ali SM, Farag HA, Konsowa AH, Elnouby M, Hamad HA (2017) Green synthesis of graphene from recycled PET bottle wastes for use in the adsorption of dyes in aqueous solution. Ecotoxicol Environ Saf 145:57–68
38. Vyazovkin S (2020) Activation energies and temperature dependencies of the rates of crystallization and melting of polymers. Polymers 12:1070
39. Brown ME, Stewart BV (1970) The thermal decomposition of ammonium metavanadate, I. J Therm Anal 2:287–299
40. Jadhav C, Pandit B, Karade S, Sankapal B, Chavan P (2018) Enhanced field emission properties of $V_2O_5$/MWCNTs nanocomposite. Appl Phys A 124:1
41. Derkaoui I, Khenfouch M, Elmokri I, Mothudi B, Dhlamini M, et al. Structural and optical properties of hydrothermally synthesized vanadium oxides nanobelts. In: Proc. IOP Conference Series: Materials Science and Engineering, 2017;186:012007
42. Venkatesan A, Nagamuthu Raja KC, Arjunan S, Marimuthu K, Mohan Kumar R, Jayavel R (2013) Structural, morphological and optical properties of highly monodispersed PEG capped $V_2O_5$- NPs synthesized through a non-aqueous route. Mater Lett 91:228–231
43. Farahmandjou M, Abaeyan N (2016) Simple synthesis of vanadium oxide ($V_2O_5$) nanorods in presence of CTAB surfactant. Colloid Surf Sci 1:10–13
44. Djennadi S, Shawagfeh N, Inc M et al (2021) The tikhonov regularization method for the inverse source problem of time fractional heat equation in the view of ABC-fractional technique. Phys Scr 96(9):094006
45. Lamsal C, Ravindra N (2013) Optical properties of vanadium oxides-an analysis. J Mater Sci 48:6341–6351
46. AbdurRahman FB, Akter M, Abedin MZ (2013) Dyes removal from textile wastewater using orange peels. Int J Sci Technol Res 2:47–50
47. Kushwaha AK, Gupta N, Chattopadhyaya MC (2017) Adsorption behavior of lead onto a new class of functionalized silica gel. Arab J Chem 10:S81–S89
48. Banerjee S, Chattopadhyaya MC (2017) Adsorption characteristics for the removal of a toxic dye, tartrazine from aqueous solutions by a low cost agricultural by-product. Arab J Chem 10:S1629–S1638
49. Ali HHM, Goher EM, Al-Afify DGA (2019) Kinetics and adsorption isotherm studies of methylene blue photodegradation under UV irradiation using reduced graphene oxide- $TiO_2$ nanocomposite in different wastewaters effluents. Egypt J Aqu Biol Fish 23:253–263
50. Ibrahim A, El Fawal GF, Akl MA (2019) Methylene blue and crystal violet dyes removal (as a binary system) from aqueous solution using local soil clay: kinetics study and equilibrium isotherms. Egypt J Chem 62:541–554
51. Abd El-Latif M, Ibrahim AM, El-Kady M (2010) Adsorption equilibrium, kinetics and thermodynamics of methylene blue from aqueous solutions using biopolymer oak sawdust composite. J Am Sci 6:267–283
52. Ahmad MA, Ahmad Puad NA, Bello OS (2014) Kinetic, equilibrium and thermodynamic studies of synthetic dye removal using pomegranate peel activated carbon prepared by microwave-induced KOH activation. Water Resour Ind 6:18–35
53. Luo W-J, Gao Q, Wu X-L, Zhou C-G (2014) Removal of cationic dye (methylene blue) from aqueous solution by humic acid-modified expanded perlite: experiment and theory. Sep Sci Technol 49:2400–2411
54. Gnanaprakasam A, Sivakumar VM, Thirumarimurugan M (2015) Influencing parameters in the photocatalytic degradation of organic effluent via nanometal oxide catalyst: a review. Ind J Mater Sci 2015:601827. https://doi.org/10.1155/2015/601827
55. Shaheen W, Abd El Maksod IH (2009) Thermal characterization of individual and mixed basic copper carbonate and ammonium metavanadate systems. J Alloys Compd 476:366–372
56. Askar M, Girgis B, Khilla M (1989) Activation energy of the thermal decomposition of ammonium metavanadate. A thermogravimetric study. J Therm Anal 35:1315–1324
57. Akande AA, Linganiso EC, Dhonge BP, Rammutla KE, Machatine A et al (2015) Phase evolution of vanadium oxides obtained through temperature programmed calcinations of ammonium vanadate in hydrogen atmosphere and their humidity sensing properties. Mater Chem Phys 151:206–214
58. Taniguchi M, Ingraham TR (1964) Mechanism of thermal decomposition of ammonium metavanadate. Can J Chem 42:2467–2473
59. Smina D, Nabil S, Omar AA (2021) A numerical algorithm in reproducing Kernel-based approach for solving the inverse source problem of the time–space fractional diffusion equation. Partial Differ Equ Appl Math 4:100164. https://doi.org/10.1016/j.padiff.2021.100164
60. Abu Arqub O, Momani S, Al-Mezel S, Kutbi M (2015) Existence, uniqueness, and characterization theorems for nonlinear fuzzy integrodifferential equations of Volterra type. Math Probl Eng 2015:835891
61. Ramana C, Hussain OM (1997) Optical absorption behaviour of vanadium pentoxide thin films. Adv Mater Opt Electron 7:225–231
62. Dreifus D, Godoy M, Rabelo A, Rodrigues A, Gobato Y et al (2015) Antiferromagnetism induced by oxygen vacancies in $V_2O_5$ polycrystals synthesized by the Pechini method. J Phys D Appl Phys 48:445002
63. Legrouri A, Baird T, Fryer J (1988) Electron optical studies of the thermal decomposition of ammonium metavanadate ($NH_4VO_3$). React Solids 5:53–68
64. Mulugeta M, Lelisa B (2014) Removal of methylene blue (Mb) dye from aqueous solution by bioadsorption onto untreated *Parthenium hystrophorous* weed. Mod Chem Appl 2:146
65. Afifah N, Saleh R. Vanadium pentoxide supported by nanographene platelets for photocatalytic application. In: Proc. AIP Conference Proceedings, 2018, 2023:020022: AIP Publishing LLC


## Publisher's Note